

Alma Mater Studiorum Università di Bologna
Archivio istituzionale della ricerca

Modeling environmental ageing in masonry strengthened with composites

This is the final peer-reviewed author's accepted manuscript (postprint) of the following publication:

Published Version:

de Miranda, S., D'Altri, A.M., Castellazzi, G. (2019). Modeling environmental ageing in masonry strengthened with composites. ENGINEERING STRUCTURES, 201(15 December 2019), 1-15 [10.1016/j.engstruct.2019.109773].

Availability:

This version is available at: <https://hdl.handle.net/11585/711905> since: 2020-04-08

Published:

DOI: <http://doi.org/10.1016/j.engstruct.2019.109773>

Terms of use:

Some rights reserved. The terms and conditions for the reuse of this version of the manuscript are specified in the publishing policy. For all terms of use and more information see the publisher's website.

This item was downloaded from IRIS Università di Bologna (<https://cris.unibo.it/>).
When citing, please refer to the published version.

(Article begins on next page)

This is the final peer-reviewed accepted manuscript of:

Stefano de Miranda, Antonio Maria D'Altri, Giovanni Castellazzi, *Modeling environmental ageing in masonry strengthened with composites*, Engineering Structures, Volume 201, 2019, 109773

ISSN 0141-0296

The final published version is available online at:

<https://doi.org/10.1016/j.engstruct.2019.109773>

© 2019. This manuscript version is made available under the Creative Commons Attribution-NonCommercial-NoDerivs (CC BY-NC-ND) 4.0 International License

(<http://creativecommons.org/licenses/by-nc-nd/4.0/>)

Modeling environmental ageing in masonry strengthened with composites

Stefano de Miranda^{1*}, Antonio Maria D'Altri¹, Giovanni Castellazzi¹

¹ Department of Civil, Chemical, Environmental, and Materials Engineering (DICAM), University of Bologna, Viale del Risorgimento 2, Bologna 40136, Italy

*corresponding author: stefano.demiranda@unibo.it

ABSTRACT

The effects of environmental ageing due to rising damp and salt crystallization on composite strengthening systems, e.g. fiber reinforced polymer (FRP) and fiber reinforced cementitious matrix (FRCM), bonded to masonry substrates are still scarcely known. Although few laboratory tests have been recently conducted to this aim, very limited information is available. In this paper, the simulation of accelerated ageing weathering cycles of masonry strengthened with composites is proposed by means of a multiphase model which accounts for salt transport and crystallization. This multiphase model is implemented together with ad hoc boundary conditions and a restart analysis procedure which attempt to reproduce the repetition of weathering cycles (composed of a wetting phase in a saline solution and a drying phase in the oven). Laboratory accelerated weathering tests on masonry specimens strengthened with lime mortar-based FRCM are numerically reproduced. Additional information on the salt crystallization process within the specimen is obtained along with the weathering procedure. Further numerical insights are shown and compared for different strengthening systems, i.e. cement mortar-based FRCM and FRP. Different salt crystallization processes in the specimens with different strengthening systems are observed and discussed.

Keywords: Salt crystallization; FRCM; FRP; Sodium chloride; Multiphase model, Durability of strengthened masonry

1 Introduction

The phenomenon of rising damp and salt crystallization is recognized as one of the major factors of environmental degradation in porous materials [1], such as masonry. Subsequent wetting and evaporation actions due to cyclic environmental conditions [2, 3] could, indeed, lead to the precipitation of salts within the material [4, 5] and, thereby, to the progressive degradation of masonry [6, 7] which could affect the structural performance of the material [8].

Additionally, masonry structures are usually strengthened due to their weak seismic performances [9], typically with externally bonded strips of composite materials [10], given their light weight and high mechanical features. Typically, fiber reinforced polymer (FRP) [11, 12, 13] and fiber reinforced cementitious matrix (FRCM) [14, 15, 16] composites are applied on masonry structures [17, 18].

In this regard, highly topical is the understanding of the durability of these strengthening systems [19] applied on masonry substrates against environmental degradation actions (as also stated in the new Italian guidelines for FRCM applications [20]), given that FRP and FRCM strengthening systems have been widespread applied on masonry buildings, even on historic monumental structures which, of course, need to be preserved along with the centuries.

Concerning the FRP strengthening system, experimental campaigns have been carried out on FRP-strengthened masonry specimens subjected to long-term hygrothermal conditions to evaluate the mechanical degradation of the bond of the FRP-masonry interface. In particular, the effect of hygrothermal conditions on durability of FRP-strengthened brick masonry was investigated in [21] through laboratory accelerated ageing tests. Furthermore, the effect of a thermo-hygrometric environment on the interface behavior of FRP-calcareous natural stones has been investigated in [22]. An overview of the durability of FRP-strengthened

masonry, with a focus on the main degradation mechanisms, available literature, and experimental backgrounds can be found in [23]. However, only very few experimental campaigns have been aimed at the evaluation of the effects of salt crystallization on the bond behavior of FRP-masonry interfaces. For example, an investigation on the influence of salt attack on the stress transfer between the FRP composite and the masonry substrate has been discussed in [24]. In particular, a negligible decrease in bond capacity of salt-conditioned specimen has been observed in [24], where crystallized salt has been found to accumulate on the sides of the composite.

Concerning the FRCM strengthening system, only few studies have been aimed at the investigation of the durability of the composite applied on masonry substrates. For example, on-site full-scale experimental tests has been carried out in [25] to evaluate the influence of aggressive environmental conditions (moisture, temperature and soluble salts presence) on the mechanical performance of FRCMs and FRPs applied on masonry substrates. Furthermore, the effect of salt crystallization on FRCMs bonded to masonry substrates has been analyzed in [26, 27, 28], where a procedure to reproduce in laboratory conditions capillary absorption and salt crystallization cycles in masonry specimens strengthened with FRCM composite strips has been developed and utilized. In particular, this accelerated weathering ageing procedure has been firstly proposed in [26], successively enhanced in [27] and tested with different types of FRCM mortar matrix in [28], showing that the matrix plays a key role in the capillary absorption of water and in the salt crystallization process. Particularly, a degradation of about the 16% in the bond strength of the conditioned specimens with respect to the unconditioned ones has been recorded in [28] for natural hydraulic lime mortar, whereas no reduction of bond strength is observed for a matrix composed of Portland cement binder and quartz sand [28].

Among the hygroscopic properties between the two families of composites, FRP strips are found to have no water vapor permeability, while FRCMs can allow water diffusion depending on the nature of their matrix. In this regard, it is generally believed that FRP reinforcements are likely generate condensation problems due to their lack of water vapor permeability, highlighting, therefore, the permeability of the composite as a positive feature.

However, although few laboratory tests have been recently conducted to evaluate the effects of salt crystallization on the durability of FRP and FRCM strengthening systems, very limited information on the crystallization phenomenon along with weathering conditions within strengthened masonry is available.

In this context, numerical models with multiphysics approaches [29] could be used to further understand these aspects. For example, a model which describes coupled heat, moisture and salt transport in porous building materials has been formulated in [30]. Moreover, the numerical modeling of salt transport and precipitation in non-isothermal partially saturated porous media accounting for kinetics of salt phase changes has been discussed in [31]. Furthermore, a model for the chemo-hydro-thermo-mechanical behavior of porous building materials considering salt transport and crystallization has been presented in [32] through a poromechanical approach. Additionally, the multiphysics modeling of spalling in bricks due to in-pore salt crystallization has been formulated in [33]. Another computational model coupling heat, water and salt ion transport, salt crystallization, deformation and damage in porous materials has been formulated in [34] and validated against neutron and X-ray imaging experimental measurements.

In this framework, part of the Authors developed in [35] a coupled multiphase model for the hygrothermal analysis of masonry structures and effective prediction of stress induced by salt crystallization. Particularly, the model has been used in [35] to reproduce the results of an experimental campaign carried out on a masonry wall exposed to weather conditions for a long time. Such model has been successively extended in [36], to account for different salt solid phases in the pores, in [37], where a fully coupling between mechanical response and moisture diffusion has been considered, and in [38], where a multi-scale approach for the analysis of mechanical effects induced by salt crystallization in porous media has been presented.

Although several advances have been achieved in the framework of multiphysics analysis of salt crystallization in masonry structures, only very few examples were aimed to the analysis of masonry strengthened with composites. For example, the modeling of moisture migration in FRP-strengthened masonry structures has

been presented in [39], and successively extended in [40, 41] to include the coupling effect of temperature gradient.

In this paper, the simulation of accelerated ageing weathering cycles of masonry strengthened with composites is proposed by means of the coupled multiphase model developed in [35], which accounts for salt transport and crystallization. This multiphase model is implemented together with ad hoc boundary conditions and a restart analysis procedure which attempt to reproduce the repetition of weathering cycles (composed of a wetting phase in a saline solution and a drying phase in the oven). Laboratory accelerated weathering tests [27] on masonry specimens strengthened with lime mortar-based FRCM are numerically reproduced. In-depth information on the salt crystallization process within the specimen are obtained along with the weathering procedure. Further numerical insights are shown and compared for different strengthening systems, i.e. cement mortar-based FRCM and FRP. Salt crystallization processes in the specimens with different strengthening systems are discussed.

The paper is organized as follows. A brief description of the coupled multiphase model utilized in the simulation is given in Section 2. The implementation of weathering cycles for masonry strengthened with composites is described in Section 3. Particularly, a brief recall of the experimental set-up used as reference is shown in Section 3.1, the definition of the weathering procedure boundary conditions is given in Section 3.2, the setting of the model parameters is shown in Section 3.3, and, finally, the results of the simulation of the weathering procedure are shown and discussed in Section 3.4. Moreover, further numerical insights on different strengthening systems are given in Section 4. The conclusions of this research work are collected in Section 5.

2 Coupled multiphase modeling of masonry

In this section, the coupled multiphase model utilized to simulate salt transport and crystallization in masonry structures, originally proposed and validated for masonry walls exposed to weather conditions in [35], is described. In the following, a brief recall of the equations and parameters involved is given.

In this modeling approach, a porous material is conceived as a multiphase continuous porous medium, which represents a system of interconnected pores within a solid matrix. The pores can be (partially) filled with a liquid phase, a gaseous phase and precipitated/crystallized salts. In general, the multiphase continuous porous medium could be constituted by three different species: (i) the material matrix (solid phase), (ii) the water (which can be in gaseous phase and/or liquid phase), and (iii) the salt (which can be dissolved, liquid phase, and/or crystallized, solid phase). The content of each component is provided by the concentration c_α^π , defined as the mass of the specie α in π -phase (m_α^π) per unit volume of the porous medium, and by the saturation degree S_α^π , defined as the pore volume occupied by the specie α in π -phase. Isothermal conditions are considered. Only one salt is supposed in the solution and, although several salt solid phases can be implemented in the model, as carried out in [36], only one salt solid phase is herein considered. Furthermore, to keep the model simple [35], the concentration of liquid water is approximated by the concentration of moisture.

In the multiphase model, the pores are considered cylindrical with isotropic distribution. Therefore, the actual pore size distribution of the porous material is not explicitly accounted for, whereas the porous material is mainly characterized by the mean pore radius and the total open porosity, and the pore size is assumed constant within the material.

The coupled multiphase model is formulated based on two balance equations together with an evolution equation. Particularly, the moisture mass conservation equation (Sec. 2.1), the salt mass conservation equation (Sec. 2.2), and the evolution equation (Sec. 2.3) which describes the salt precipitation/dissolution kinetics, are conceived. Three independent primary variables govern the multiphase phenomena: (i) the pore relative humidity h (defined as the ratio between the actual vapor pressure and the vapor pressure at saturation), (ii) the mass fraction of the dissolved salt ω , (iii) and the concentration of crystallized salt per unit volume of porous medium c_s^s .

2.1 Moisture mass conservation

The moisture mass conservation can be written as:

$$\frac{\partial c_w}{\partial t} + \nabla \cdot \mathbf{j}_w = 0 \quad (1)$$

where c_w is the concentration of moisture, \mathbf{j}_w is the water flux (i.e. $\mathbf{j}_w = \mathbf{j}_w^g + \mathbf{j}_w^l$, being \mathbf{j}_w^g the water vapor flux and \mathbf{j}_w^l the water liquid flux), and the operator $\frac{\partial}{\partial t}$ represents a time derivative.

2.2 Salt mass conservation

The salt mass conservation can be written as:

$$\frac{\partial c_s^l}{\partial t} + \nabla \cdot \mathbf{j}_s^l + \frac{\partial c_s^s}{\partial t} = 0 \quad (2)$$

where c_s^l is the concentration of liquid salt and \mathbf{j}_s^l is the flux of dissolved salt. Furthermore, \mathbf{j}_w^l and \mathbf{j}_s^l can be written as:

$$\mathbf{j}_w^l = (1 - \omega)\mathbf{j}_{ws}^l - \mathbf{j}_{s,diff}^l \quad (3)$$

$$\mathbf{j}_s^l = \omega\mathbf{j}_{ws}^l - \mathbf{j}_{s,diff}^l \quad (4)$$

where \mathbf{j}_{ws}^l is the flux of the liquid phase and $\mathbf{j}_{s,diff}^l$ is the diffusive flux of the dissolved salt.

2.3 Evolution equation

The salt crystallization or dissolution is assumed to be governed by the supersaturation ratio ω/ω_{sat} , i.e. the ratio between the current concentration of dissolved salt ω and the concentration at saturation ω_{sat} . Crystallization starts when the supersaturation ratio is greater than the threshold α_0 and dissolution starts when the supersaturation ratio is less than one:

$$\begin{cases} \frac{\omega}{\omega_{sat}} > \alpha_0 \Rightarrow \text{crystallization} \\ \frac{\omega}{\omega_{sat}} < 1 \Rightarrow \text{dissolution} \end{cases} \quad (5)$$

For primary crystallization $\alpha_0 > 1$, but when the first salt crystal appears in the pores, further crystallization proceeds at $\alpha_0 = 1$. In general, the threshold of supersaturation ratio for primary crystallization relies on the properties of the porous material and on the type of salt. Indeed, in [42], α_0 for primary crystallization varies depending on the type of brick (i.e. the pore size distribution and, so, the mean pore radius) and on the type of salt (for the same brick, it can varies, for example, from 1.75 in case of sodium sulphate to 1.03 in case of potassium chloride [42]). Therefore, a very accurate value of this threshold should be carefully evaluated experimentally for each specific case. However, given that its influence on the overall response appears not particularly significant (as also experienced by the Authors for values comprised between 1 and 1.7), it is common to adopt a unit value also for the threshold of supersaturation ratio for primary crystallization [42, 35, 43, 44]. This value has been used also in the following.

The evolution equation which describes the salt precipitation/dissolution kinetics, i.e. it quantifies the amount of salt which precipitates, can be written as:

$$\frac{\partial c_s^s}{\partial t} = \pi r_p^2 \rho_s^s \frac{n}{V_{tot}} K_c \left| \frac{\omega}{\omega_{sat}} - 1 \right|^P \quad (6)$$

where a constant amount of salt nuclei n in the solution, as well as an isotropic distribution of cylindrical pores and cylindrical nuclei of the same radius of the pores (r_p), is assumed. In (6), ρ_s^s is the density of the crystallized salt, K_c is the growth rate coefficient, V_{tot} the pore volume, ω_{sat} the concentration of dissolved salt at saturation, and P is the crystallization process order that relies on the properties of the porous material and on the type of salt. Various scientific works adopted different values of P for brick. For example, $P = 1$ has been adopted in [42] for diffusion-forced hydration processes. Other approaches adopted $P = 1$ for sodium chloride (e.g. in [35]), while in [36] (for sodium sulphate) $P = 1$ has been adopted for Mirabilite crystallization, while $P = 1.5$ has been adopted for Thenardite V crystallization. Furthermore, the use of $P = 1.5$ has been suggested in [43] for sodium sulphate after an inverse problem determination through experimental data. A sensitivity analysis has been preliminary conducted by the Authors to highlight the influence of the crystallization process order P in the salt crystallization within the porous material, although $P = 1$ is generally assumed for sodium chloride [35]. As a result, the value of P influences the amount of precipitated salt recorded in the drying phases, with no significant differences in the wetting phases. Particularly, the concentration of solid salt tends to decrease in the drying phase while increasing the value of P , confirming the trend highlighted in [43]. However, values of $1 \leq P \leq 1.5$ would not overturn the core of

the results (i.e. with differences with respect to the case $P = 1$ included within the engineering accuracy tolerance), and $P = 1$ is adopted in the following.

2.4 Constitutive equations

The following constitutive equations are adopted to define the gas flow, the capillary liquid flow and the diffusive flux of dissolved salt, respectively:

$$\mathbf{j}_w^g = -K_g \nabla p_v, \quad (7)$$

$$\mathbf{j}_{ws}^l = -K_l \nabla p_c, \quad (8)$$

$$\mathbf{j}_{s,diff}^l = -\rho_{ws}^l K_s \nabla \omega, \quad (9)$$

where K_g is the vapor permeability, K_l the liquid permeability of the salt solution, K_s the salt diffusion coefficient, p_v the vapor pressure, p_c the capillary pressure, and ρ_{ws}^l the mass density of the liquid phase.

The vapor permeability K_g can be written as:

$$K_g = \frac{D_v}{R_v T} \quad (10)$$

where D_v is the vapor permeability coefficient and R_v is the gas constant of water vapor (0.4615 kJ/kg/K).

The liquid permeability of the salt solution can be expressed as:

$$K_l = g_\omega D_l S_{ws}^l \quad (11)$$

where D_l is the liquid conductivity of pure water, S_{ws}^l is the saturation degree of the solution and g_ω is a correction function which accounts for the presence of salt in the solution. The expression developed in [45] is utilized:

$$D_l = \frac{h}{\rho_w^l R_v T} \left[3.8 \left(\frac{A}{\phi_0 \rho_w^l} \right)^2 10^{3(S_w^l - 1)} \right] \frac{\partial c_w}{\partial h} \quad (12)$$

being A the adsorption coefficient of the material, and ϕ_0 the initial porosity of the material. The expression of g_ω is assumed, in agreement with [36], as:

$$g_\omega = \frac{\rho_{ws}^l}{\rho_w^l} (1 - 0.03m) \quad (13)$$

where m is the molality of the solution.

The effect of salt precipitation on the gas and liquid conductivity is accounted for by changing the expressions of K_g and K_l by means of correcting functions (g_g and g_l , respectively) which depend on the effective porosity ϕ_{eff} :

$$K_g \leftarrow g_g(\phi_{eff}) K_g, \quad K_l \leftarrow g_l(\phi_{eff}) K_l, \quad (14)$$

being

$$\phi_{eff} = \phi_0(1 - S_s^s) \quad (15)$$

where ϕ_0 is the initial porosity and S_s^s the saturation degree of crystallized salt. Analogously to [44], the simple assumption of $g_g = g_l = 1 - S_s^s$ is made. Finally, the value of the salt diffusion coefficient K_s should depend on the actual cross section available for diffusion. By taking this into account, K_s is assumed to be dependent on the saturation degree of the solution S_{ws}^l , i.e. its definition becomes:

$$K_s \leftarrow K_s \cdot S_{ws}^l. \quad (16)$$

The saturation degree of the solution S_{ws}^l can be expressed as function of the relative humidity h through the sorption/desorption curve $S_{ws}^l(h)$ (assumed in this study as in [35]).

The vapor pressure and the capillary pressure in (7) and (8), respectively, can be expressed as:

$$p_v = p_{v,sat} h \quad (17)$$

$$p_c = \rho_w^l R_v T \ln(h) \quad (18)$$

where $p_{v,sat}$ is the saturation vapor pressure of the salt mixture, which depends on the temperature and the dissolved salt concentration, and ρ_w^l is the mass density of liquid water.

2.5 Boundary conditions

The formulation of the model is completed by the boundary conditions. Boundary conditions can be of Dirichlet's type:

$$h = \bar{h}, \quad (19)$$

$$\omega = \bar{\omega}, \quad (20)$$

and of Neumann's or Robin's type:

$$\mathbf{j}_w \cdot \mathbf{n} = q_w + \gamma_w (A_w h - h_\alpha), \quad (21)$$

$$\mathbf{j}_s^l \cdot \mathbf{n} = q_\omega, \quad (22)$$

being \mathbf{n} the outward unit normal to the boundary, \bar{h} and $\bar{\omega}$ the prescribed humidity and salt concentration, respectively, q_w and q_ω , the prescribed normal fluxes of moisture and salt, respectively, h_α the prescribed environmental humidity, A_w the water activity, and γ_w the convective humidity coefficient.

2.6 Model implementation

The differential equations adopted in the model are fully coupled and highly nonlinear. A standard iterative strategy based on the Newton-Raphson method has been applied to solve the non-linear system of equations. The time discretization has been performed through the backward finite difference method. This model has been implemented in COMSOL Multiphysics [46] using finite elements with quadratic shape functions.

3 Implementation of weathering cycles for masonry strengthened with composites

In this section, the simulation of weathering cycles laboratory tests on masonry specimens strengthened with FRCM made of natural hydraulic lime (NHL) mortar is presented. Firstly, the laboratory accelerated weathering tests are briefly described. Then, the boundary conditions assumed in the model to simulate the weathering procedure are defined, as well as the setting of the model parameters. Finally, the numerical results obtained by simulating the weathering tests are critically discussed.

3.1 Laboratory accelerated weathering tests

Four brick masonry specimens with six half-bricks ($125 \text{ mm} \times 120 \text{ mm} \times 380 \text{ mm}$) joined by five 10 mm-thick mortar layers were reinforced with FRCM strips (Fig. 1), made of galvanized steel fibers embedded within NHL mortar, and were subjected to the artificial weathering procedure designed in [27], involving capillary salt solution absorption and salt crystallization cycles. The material properties of the solid fired-clay bricks and of the dry-mix commercially available mortar employed for the joints are collected in [27], as well as the properties of the composite utilized.

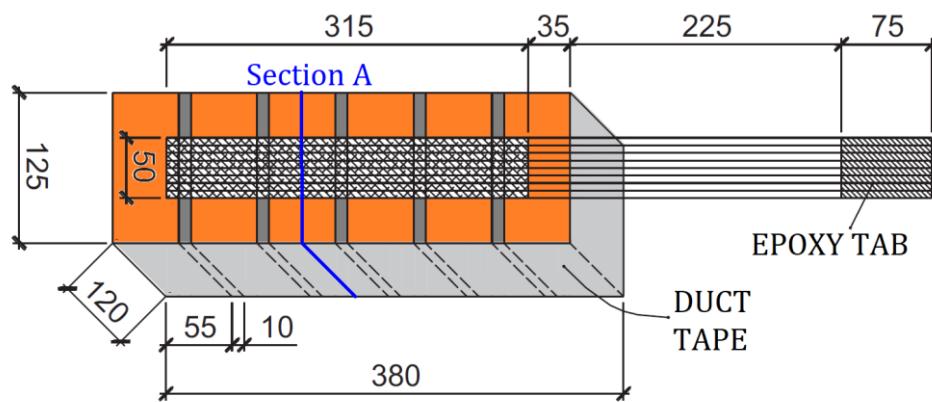


Fig. 1 – Specimen used in the weathering procedure. Measures in mm.

After the assembly of the masonry specimens, they were cured in laboratory conditions for one month. Then, the application of the composite on one face of the masonry specimens was carried out. Firstly, a layer (thickness 4 mm) of commercially available dry-mix natural hydraulic lime-based mortar with quartz sand was applied on one face of the specimen. Then, a steel fiber sheet consisting in a unidirectional sheet made of ultra-high strength galvanized steel cords, fixed to a secondary 6 mm-spaced fiberglass micromesh, was applied and carefully pressed into the first matrix layer. Finally, a second 4 mm-thick layer of matrix was applied onto the steel fiber sheet. The total thickness of the FRCM composites resulted equal to 8 mm. The specimen is sketched in Fig. 1.

The weathering procedure consists of six cycles each one composed of a wetting phase in a saline solution followed by a drying phase. In the wetting phase, the specimens were partially immersed in an aqueous solution of sodium chloride, NaCl (4 wt%), with a solution head of 20 mm for 48 hours at laboratory temperature (i.e. an average value of $27 \text{ }^\circ\text{C}$). The wetting phase was followed by a drying phase in a ventilated oven at $60 \text{ }^\circ\text{C}$ for 48 hours. A sketch of one cycle of the weathering procedure is shown in Fig. 2. In order to have evaporation through the top surface (the one to which the composite was applied), a duct tape was applied to the four lateral faces of the specimens (Fig. 1).

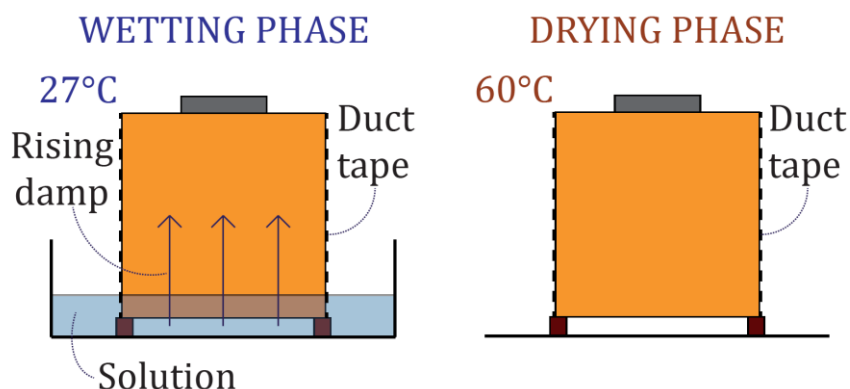


Fig. 2 – Sketch of one cycle of the weathering procedure: wetting phase (48h) and drying phase (48h).

The accelerated weathering protocol was designed to reproduce, in a relatively short period of time, salt crystallization cycles and achieve realistic concentrations of salts in the masonry specimens, i.e. amounts that can be found in real historical buildings [27]. It has to be pointed out that, in general, salt crystallization patterns significantly depend on the velocity of the weathering processes. Accordingly, fully consistent tests should reproduce the same velocities of actual weathering processes. However, this is typically not feasible for technical and practical reasons. Therefore, the recourse to accelerated weathering protocols is generally accepted in the scientific community [26, 28], even though their definition is a challenging task. In the framework of the RILEM Technical Committee TC-ASC “*Accelerated laboratory test for the assessment of the durability of materials with respect to salt crystallization*”, the important aspects to be considered in setting-up accelerated weathering cycles to reproduce salt crystallization that occurs in the field have been highlighted [47].

Fig. 3 shows the four specimens at the end of the weathering procedure. As can be noted, efflorescence is substantially distributed over the entire top surface of the specimen, including the FRCM composite.

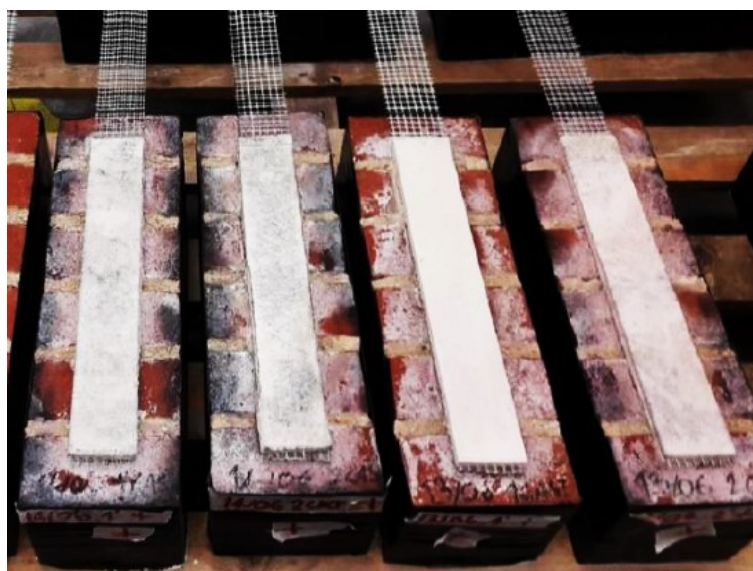


Fig. 3 – Photo of four specimens after the weathering cycles.

After the weathering procedure, samples of material were collected by chisel fragmentation from Section A (Fig. 1). Fragments from three different locations in the specimen (two in the brick, B-L and B-C, and one in the composite matrix, M-C, see Fig. 4(a)) were extracted from two specimens. Particularly, brick samples were

taken beneath the top surface at two locations that correspond, respectively, to the center and edge of the specimen. Anyway, all the fragments were collected sufficiently far from the edges. Salts concentrations were determined on the fragments by grinding to powder, extraction with deionized boiling water, filtration by blue ribbon filter, and ion chromatography (IC) [27].

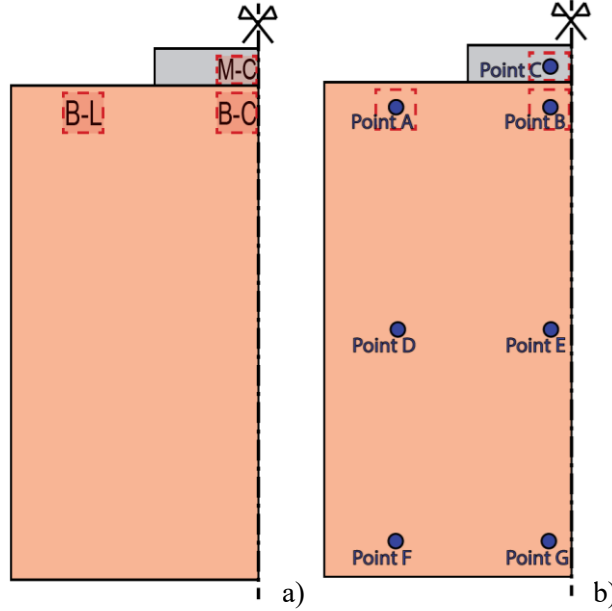


Fig. 4 – (a) Regions of extraction of samples, referred to Section A of Fig. 1, and (b) points selected in the numerical model.

3.2 Definition of the boundary conditions

A cross section of the specimen (Section A, Fig. 1) is considered in the numerical simulations. In particular, only one half of the cross section is conceived for symmetry reasons. Boundary conditions are one-after-the-other applied to simulate the weathering procedure. In particular, two sets of boundary conditions are applied to model the weathering cycle (Fig. 5): one for the wetting phase and one for the drying phase.

In the wetting phase ($T = 27^{\circ}\text{C}$), Dirichlet's boundary conditions are applied to the bottom side reproducing the immersion in saline solution, i.e. $h = 100\%$ and $\omega = 4\%$. Conversely, liquid water flux equal to $\mathbf{j}_w^l \cdot \mathbf{n} = \gamma_w(A_w h - h_{wet})$ and zero flux of dissolved salt are assumed on the top side of the domain. In the drying phase ($T = 60^{\circ}\text{C}$), Neumann's boundary conditions with liquid water flux equal to $\mathbf{j}_w^l \cdot \mathbf{n} = \gamma_w(A_w h - h_{dry})$ and zero flux of dissolved salt are assumed in both bottom and top sides. Zero liquid water and dissolved salt fluxes are assumed in the vertical sides (in the external one due to the presence of the duct tape and in the central one due to symmetry reasons). In the wetting phase, the averaged measured value of environmental humidity $h_{wet} = 56\%$ is used, while the value $h_{dry} = 20\%$ is assumed in the drying phase.

The convective humidity coefficient γ_w depends on the concentration of crystallized salt. In agreement with [44], γ_w is assumed to be dependent on c_s^s through a bi-exponential function tuned basing on drying experiments. The value of γ_w for a condition of zero crystallized salt ($c_s^s = 0$) is assumed equal to $0.4 \text{ kg/m}^2/\text{s}$, following the outcomes obtained in [35] for ventilated conditions. By incrementing the magnitude of crystallized salt, γ_w can decrease till a residual value equal to the 20% of the initial value. The water activity A_w is function of ω and depends on the type of salt. Following [44] for sodium chloride, A_w is assumed equal to 1 when $\omega = 0$ and equal to 0.75 when $\omega \geq \omega_{sat}$.

A restart analysis procedure is implemented in COMSOL Multiphysics [46] to simulate the weathering procedure. In this way, the domain values of the three independent variables at the end of the wetting phase

become the initial domain values for the drying phase and so on. The whole domain initial values (i.e. at the beginning of the weathering procedure) are assumed to be $h = 50\%$, $\omega = 0$ and $c_s^s = 0$.

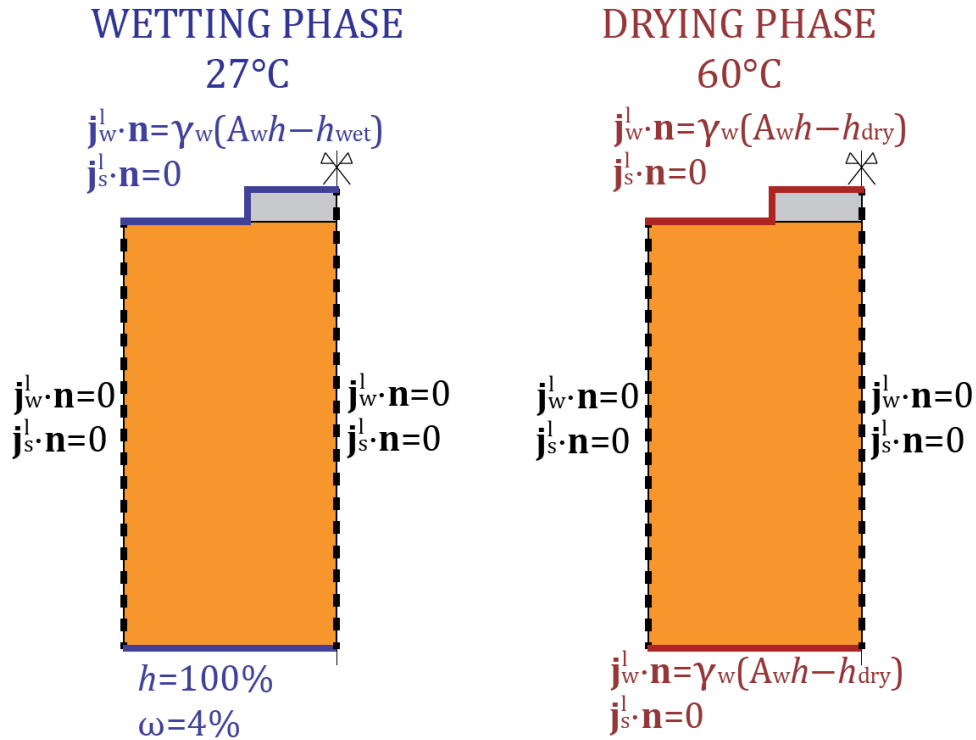


Fig. 5 – Sketch of the boundary conditions adopted in the modeling approach for the wetting phase and the drying phase of the weathering procedure.

3.3 Setting of the model parameters

Several model parameters and material properties are needed to characterize the model described in Section 2. Therefore, the setting of the model parameters is a challenging task. However, several laboratory tests were carried out in [35, 27, 28] to experimentally characterize some model parameters. In particular, many of them were defined and calibrated in [35], where the same type of red fired clay-brick was conceived. Furthermore, the material characterization of the NHL mortar has been conducted in [28], where the main material properties have been defined. Lastly, some parameters were also taken from the literature. The summary of the model parameters is shown in Table 1.

Table 1. Summary of the model parameters.

Quantity	Value	Source
K_c Growth rate coefficient	0.03 $\mu\text{m/s}$	Refs. [48, 49]
n Nuclei in solution	$4 \cdot 10^{-6} (\mu\text{m}^3)^{-1}$	Ref. [42]
P Crystallization process order	1	Ref. [44]
ω_{sat} Concentration of dissolved salt at saturation	0.264 kg/kg	Refs. [35, 44, 50]
D_v Vapor permeability coefficient	0.0039 m^2/h	Ref. [45]
α_0 Crystallization threshold	1	Ref. [42]
ρ_s^s Solid NaCl density	2160 kg/m^3	Literature

Brick			
r_b	Mean pore radius	0.700 [μm]	Ref. [35]
ϕ_0	Initial porosity	26.0%	Ref. [35]
A	Water adsorption coefficient	0.185 [$\text{kg}/\text{m}^2/\text{s}^{0.5}$]	Ref. [35]
K_s	Salt diffusion coefficient	$0.499 \cdot 10^{-9}$ [m^2/s]	Ref. [35]
NHL			
r_b	Mean pore radius	0.491 [μm]	Ref. [28]
ϕ_0	Initial porosity	26.6%	Ref. [28]
A	Water adsorption coefficient	0.054 [$\text{kg}/\text{m}^2/\text{s}^{0.5}$]	Ref. [28]
K_s	Salt diffusion coefficient	$0.120 \cdot 10^{-9}$ [m^2/s]	Ref. [51]

Before proceeding to the simulation of the full weathering procedure, a simple wetting test with pure water was performed and compared to experimental outcomes to evaluate the consistency of the parameters (which govern the water diffusion phenomenon) used in the simulations. The domain shown in Fig. 5 was discretized by means of quadratic triangular FEs as shown in Fig. 6. In particular, a mesh refinement was conceived in the top part of the domain (Fig. 6) as it was found, through preliminary analyses, to be a region with a great gradient of the independent variables.

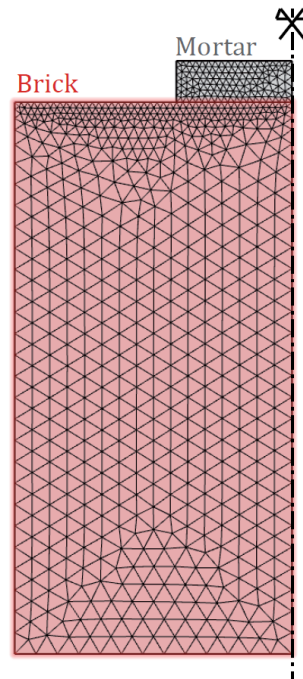


Fig. 6 – Mesh adopted in the simulations: quadratic triangular FEs (10,071 DOFs).

The simulation of the wetting test has been carried out assuming the boundary conditions expressed in Fig. 5 for the wetting phase and considering, however, the Dirichlet's condition $\omega = 0\%$ at the bottom side of the specimen to reproduce pure water. The evolution of the pore relative humidity h along with time is shown in Fig. 7 in terms of h -contour plots at subsequent time instants (0h, 0.5h, 1h, 2h, 24h, and 48h). Moreover, Fig. 8 shows the comparison between experimental measures and numerical outcomes for the evolution of the relative humidity in the wetting phase, in terms of percentage of wet specimen. In this case, the experimental

data were deduced by subsequent weighing of the specimen at certain time instants. In particular, the experimental outcomes of three different wetting tests were reported in Fig. 8. As can be noted in Fig. 8, the specimen substantially appears fully-saturated after around 4 hours in the numerical simulation. This outcome appears reasonably in agreement with the experimental results, as shown in Fig. 8.

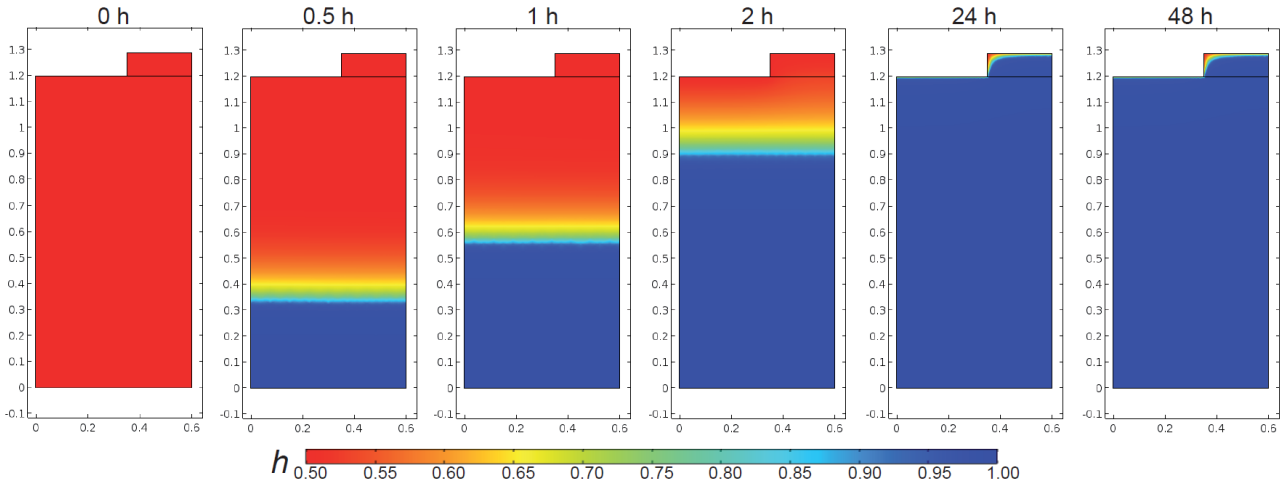


Fig. 7 – Evolution of the pore relative humidity h in the wetting test with pure water. Measures in $\text{cm} \cdot 10^1$.

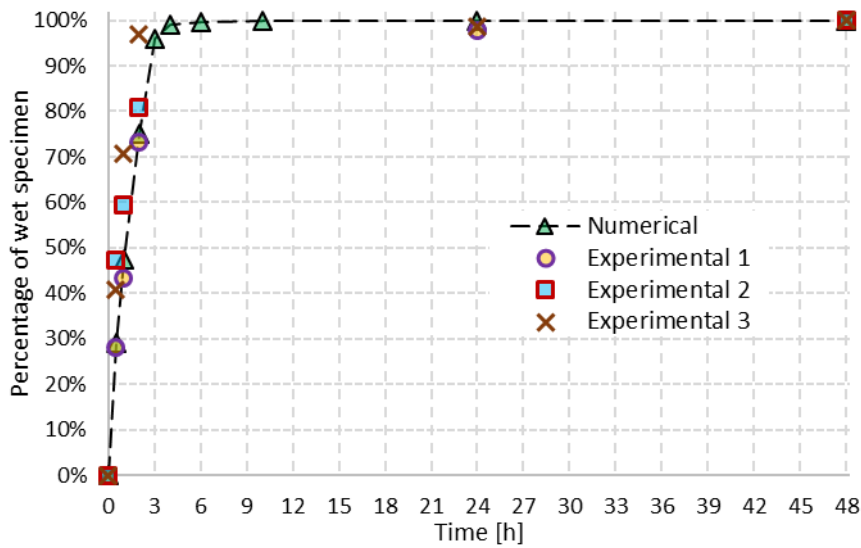


Fig. 8 – Comparison between experimental measures and numerical outcomes for the evolution of the relative humidity in the wetting test with pure water.

3.4 Simulation of the weathering procedure

The full weathering procedure (six cycles each one composed of a wetting phase and a drying phase of 48 hours each) defined in [27] with a solution of NaCl (4 wt%) has been simulated by using the boundary conditions shown in Fig. 5, the model and material properties illustrated in Section 3.2, and the restart analysis procedure implemented as described in Section 2.5. The points highlighted in Fig. 4(b) are conceived to monitor the evolution of crystallized salt along with the conditioning. In total, twelve 48-hours simulations have been performed one after the other, alternating wetting phases and drying phases.

The evolution of crystallized salt c_s^S along with the conditioning is shown in Fig. 9 with reference to the seven points highlighted in Fig. 4(b). By inspecting Fig. 9 it appears that:

- The points in the top part of the specimen (points A and B in the brick and point C in the composite matrix) tends to accumulate crystallized salt along with the conditioning (both in brick and composite matrix). Particularly, the concentration of crystallized salt c_s^S increases rapidly in the very first part of the drying phase, remaining substantially constant in the rest of the drying phase. Then, c_s^S tends to decrease in the first four hours of the subsequent wetting phase (more significantly for point B rather than points A and C). Anyway, the amount of crystallized salt which is dissolved in the wetting phases is lower than the amount of salt that crystallizes in the drying phases. In this way, an accumulation phenomenon of c_s^S in points A, B and C can be observed. At the end of the weathering procedure, the amount of salt crystallized in the points A, B and C appears similar (between 85 and 95 kg/m³), with, however, a greater value of crystallized salt in point B, i.e. in the brick just beneath the composite matrix.
- The points in the central part of the specimen (points D and E) show salt crystallization in the first part of the drying phase (with few hours of delay with respect to points A, B and C), with an amount of crystallized salt (around 22 kg/m³) even greater than points A, B and C for the first drying phase. However, the crystallized salt in points D and E is completely dissolved in the first hours of the subsequent wetting phase. Therefore, no accumulation phenomenon is recorded in this part of the specimen.
- The points in the bottom part of the specimen (points F and G) show a similar behavior of points D and E, with the difference that the amount of crystallized salt in the drying phase is significantly lower, i.e. around 2 kg/m³.

The c_s^S contour plots at the end of each phase are collected in Fig. 10. These plots make clearer the aspects already discussed for Fig. 9, i.e. in the top part of the specimen there is accumulation of crystallized salt (one cycle after the other), while in the central part of the specimen the salt crystallized in the drying phase is completely dissolved in the subsequent wetting phase.

It is worth to note that a very thin layer with high concentration of crystallized salt appears in the very top part of the specimen at the end of the 2nd cycle wetting phase, and it remains (by increasing the amount of crystallized salt) for the rest of the weathering procedure (Fig. 10). Particularly, this very thin layer locates in a zone characterized by a high gradient of pore relative humidity h in the wetting phase (see Fig. 7 at 24h and 48h). Coarsely, this thin layer with a high concentration of crystallized salt (Fig. 10) locates in the border between dry and wet material (Fig. 7). Substantially, this thin layer represents, in some way, a salt crust very close to the top boundary of the specimen, i.e. the surfaces of the specimen directly exposed to environmental conditions.

As mentioned in Section 3.1, fragments from three different locations in the specimen (two in the brick, B-L and B-C, and one in the composite matrix, M-C, see Fig. 4(a)) were extracted in laboratory at the end of the conditioning and processed through IC to compute the amount of salt in the materials. The values of concentration of salts measured through IC in the B-L, B-C and M-C regions are compared with the numerical outcomes in Fig. 11 (being negligible the amount of liquid salt after the drying phase). Particularly, Fig. 11 shows the numerical evolution of the concentration of crystallized salt in the regions B-L, B-C and M-C, considering the maximum and minimum values of the crystallized salt which can be found in these regions, and the values experimentally measured through IC at the end of the weathering procedure. As can be noted in Fig. 11, a significant difference could be observed between the maximum and minimum numerical values obtained within the regions B-L, B-C and M-C. In particular, this difference is significantly remarkable for zone B-C (Fig. 11), that, indeed, shows a considerable gradient of crystallized salt (Fig. 10). A reasonable agreement could be observed in Fig. 11 by comparing the numerical envelopes with the experimental measurements. Indeed, the experimental values are generally included within the numerical envelopes, although the experimental value M-C1 is slightly lower than the lower numerical bound.

Typically, the experimental measurements of crystallized salt concentration locate nearer the lower numerical bound rather than the upper one (Fig. 11). This outcome appears reasonable as the experimental boundary condition cannot be considered perfect (for obvious reasons, e.g. the duct tape used in the lateral surfaces

sometimes showed detachment from the masonry substrate as discussed in [27]), while, instead, the numerical boundary conditions are rigorously applied.

In conclusion, the numerical model used to simulate weathering cycles of masonry strengthened with NHL-based FRCM appears quantitatively consistent with experimental measures, as shown in Fig. 11 for the concentration of crystallized salt.

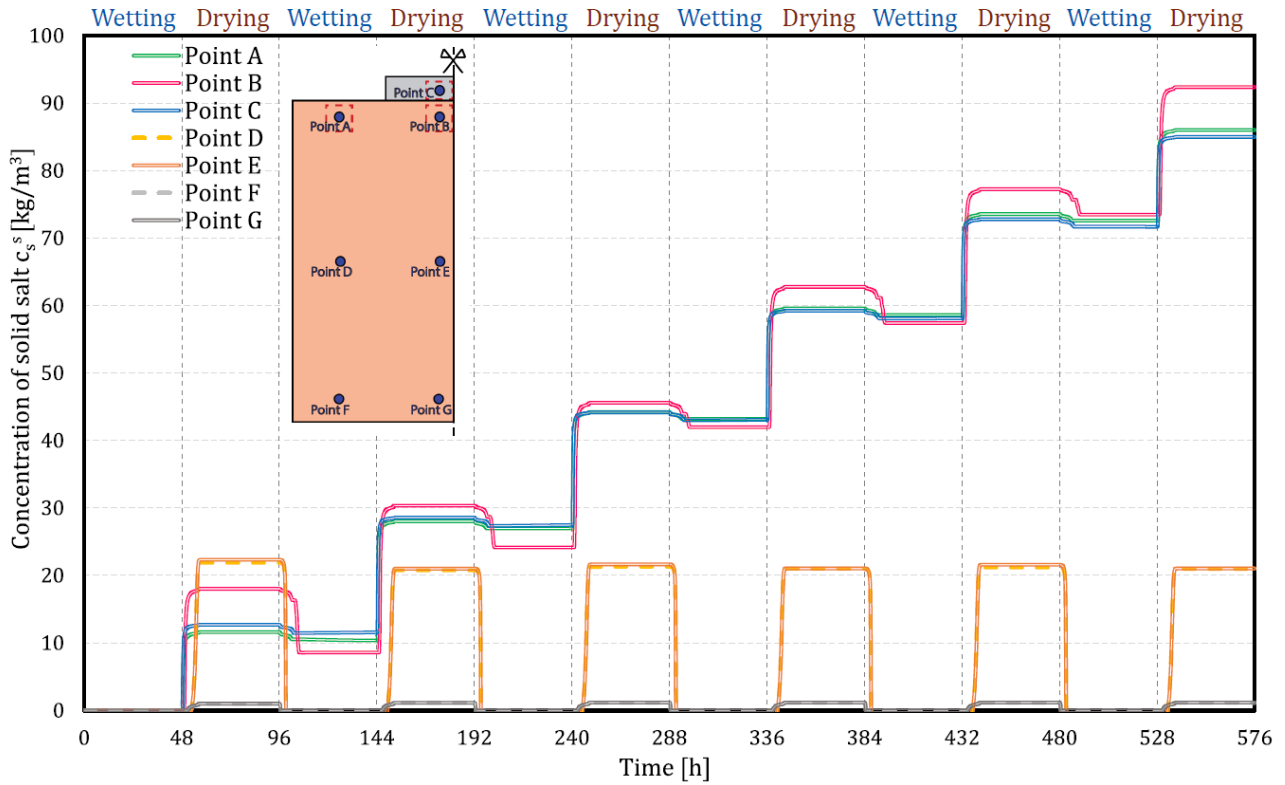


Fig. 9 – Evolution of crystallized salt along with the conditioning (NHL specimen).

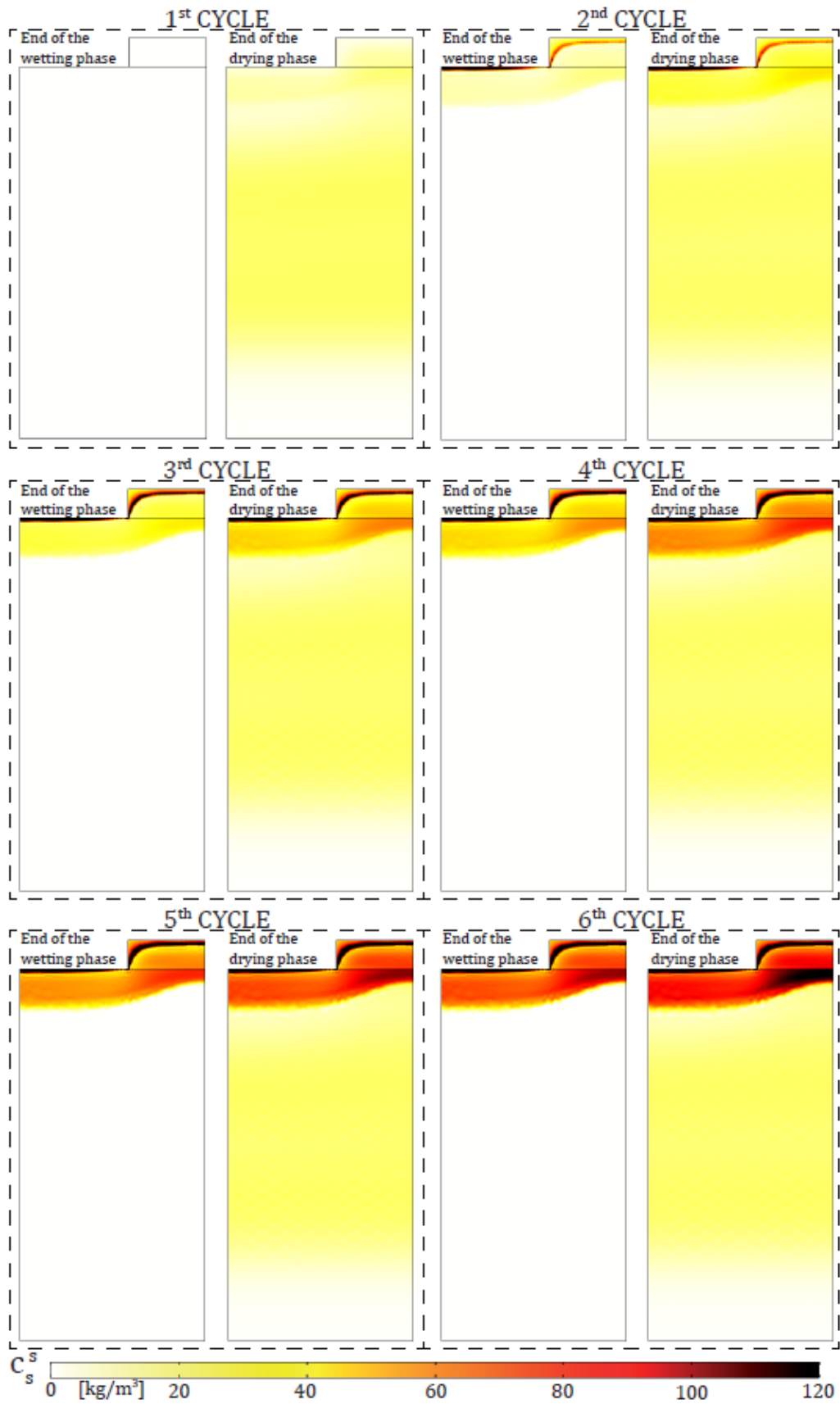


Fig. 10 – Evolution of salt crystallization within the NHL specimen.

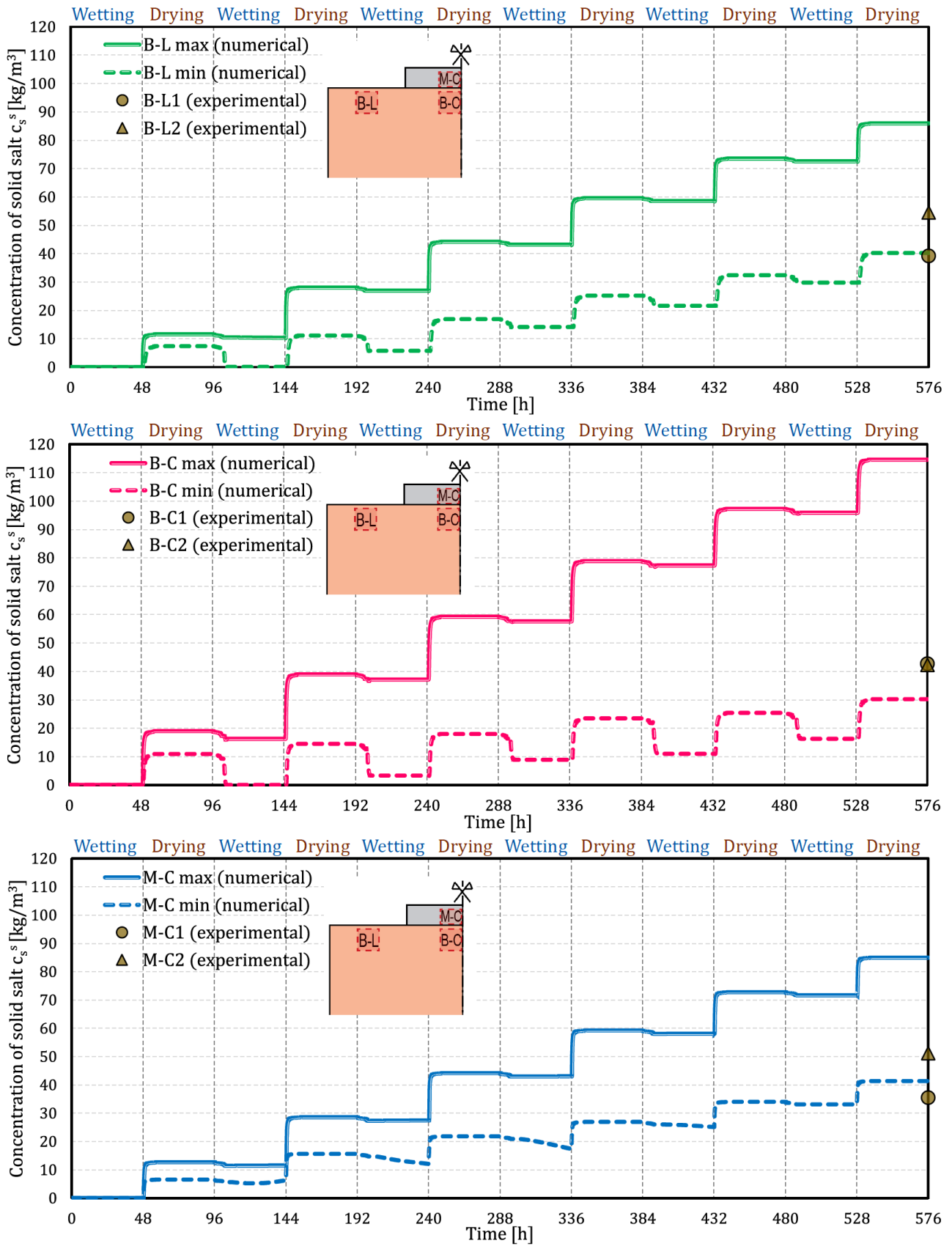


Fig. 11 – Evolution of the concentration of crystallized salt in the regions B-L, B-C and M-C. The experimental values are referred to Section A of Fig. 1 (NHL specimen).

4 Further numerical insights on different strengthening systems

In this section, the model and the numerical procedure presented in the previous sections are used to investigate the effects of the conditioning of strengthened masonry on different strengthening systems. Particularly, the weathering procedure applied on masonry strengthened with NHL-based FRCM is compared with two other strengthening systems, keeping unchanged the other model parameters: (i) FRCM made of a matrix composed of Portland cement binder and quartz sand (CEM) and (ii) FRP.

The mechanical properties of the CEM matrix are collected in [28] and the main material properties which characterize the multiphase numerical model are shown in Table 2, where they are compared against the NHL ones. As can be noted in Table 2, the two materials are sensibly different from a hygroscopic point of view. Indeed, for example, their mean pore radius r_b has one order of magnitude of difference.

Conversely, the FRP strengthening system is modeled as an impermeable membrane (i.e. through a zero-flux boundary condition $\mathbf{j}_w^l \cdot \mathbf{n} = 0$, $\mathbf{j}_s^l \cdot \mathbf{n} = 0$), given its hygroscopic properties and its coupling with epoxy resin [24].

Table 2. Matrix properties of NHL and CEM mortars.

Mortar	Mean pore radius r_b [μm]	Initial porosity ϕ_0 [%]	Water adsorption coef. A [$\text{kg}/\text{m}^2/\text{s}^{0.5}$]	Salt diffusion coef. K_s [m^2/s]
NHL	0.491 (from [28])	26.6% (from [28])	0.054 (from [28])	$0.120 \cdot 10^{-9}$ (from [51])
CEM	0.041 (from [28])	22.5% (from [28])	0.020 (from [28])	$0.020 \cdot 10^{-9}$ (from [52])

The comparison of the evolution of crystallized salt along with the conditioning between NHL, CEM and FRP strengthening systems is shown in Fig. 12 for the points A, B and C of Fig. 4(b) (obviously, point C does not exist in the FRP case). By inspecting Fig. 12 it appears that:

- Concerning point A, all cases (NHL, CEM and FRP) show accumulation of crystallized salt along with the conditioning. Moreover, the curves of the three cases are rather similar in point A.
- Concerning point B, the three strengthening systems show significantly different responses. On the one hand, NHL shows accumulation in point B similarly to point A. On the other hand, either CEM or FRP show crystallization and complete dissolution for each drying and wetting phase, respectively, following a similar behavior of point D and E of Fig. 9. In point B, the crystallized salt is substantially equal in CEM and FRP for the first drying phase, whereas it is slightly greater in CEM rather than in FRP in the following drying phases. Therefore, the accumulation of crystallized salt in the brick just beneath the composite is only recorded in the NHL strengthening system.
- Concerning point C, NHL and CEM show a completely different behavior. On the one hand, the accumulation in the NHL case is similar to point A, with a magnitude of about $85 \text{ kg}/\text{m}^3$ at the end of the conditioning. On the other hand, the CEM case does not show significant accumulation in point C, with a magnitude of about $2 \text{ kg}/\text{m}^3$ at the end of the conditioning. This outcome appears sensibly interesting as for the same type of strengthening system (i.e. FRCM), but different matrixes (i.e. NHL and CEM), the weathering procedure induces completely different concentrations of crystallized salts in the two matrixes.

Summing up the results, the response of the CEM case appears more similar to the FRP case rather than the NHL case, i.e. no accumulation of crystallized salt is recorded in the brick just beneath the composite and no salt crystallizes within the composite.

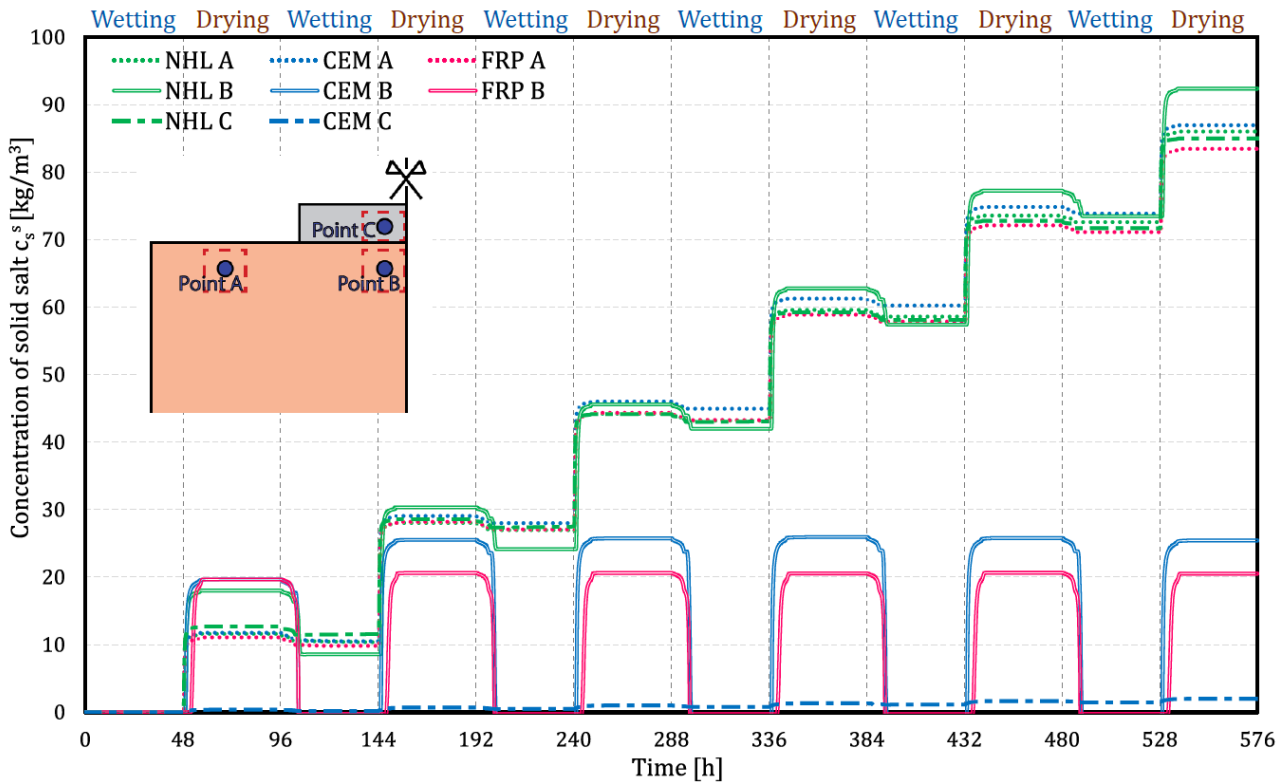


Fig. 12 – Comparison of the evolution of crystallized salt between the NHL, CEM and FRP strengthening systems in points A, B, and C (Fig. 4(b)).

The c_s^s contour plots at the end of each phase are collected in Fig. 13 and Fig. 14 for the NHL, CEM and FRP strengthening systems (in Fig. 13 the first three cycles and in Fig. 14 the last three cycles). Once again, these plots make clearer the aspects already discussed in Fig. 12. Indeed, the pattern of accumulation of crystallized salt in the top part of the specimen is sensibly different between the three strengthening systems (Fig. 13 and Fig. 14):

- In the NHL case, a significant amount of salt arises both in the brick (lateral part and beneath the composite) and in the composite matrix (with similar amount of salts which increase one cycle after the other).
- In the CEM case, no significant salt crystallization is observed in the composite matrix and in the brick just beneath the composite matrix (in the central part), even if significant salt crystallization and accumulation (comparable to the one in the lateral part of the brick) appears in the brick beneath the lateral extremity of the composite. Coarsely, a significant amount of accumulated crystallized salt is observed in about 30% of the brick portion just beneath the composite matrix.
- In the FRP case, no significant crystallized salt accumulation is observed in all the portion of brick just beneath the composite strip. Salt crystallization and accumulation only arises in the top part of the brick which is not covered by the composite.

This outcome appears qualitatively in agreement with the experimental observations collected in [28], even though in [28] different saline solutions were conceived. Indeed, in [28] a considerable amount of salt was found in the NHL matrix, whereas no significant salt crystallization was observed in the CEM matrix, for the same weathering procedure.

A very thin layer with high concentration of crystallized salt also appears in the very top part of the uncovered brick only, and not also in the composite matrix as in the NHL case, at the end of the 2nd cycle wetting phase for both CEM and FRP cases, (Fig. 13 and Fig. 14). Finally, the central and bottom parts of the specimen show a similar behavior (crystallization and complete dissolution) in every case (Fig. 13 and Fig. 14).



Fig. 13 – Comparison of the evolution of salt crystallization within specimens strengthened with different composite systems. First three cycles.

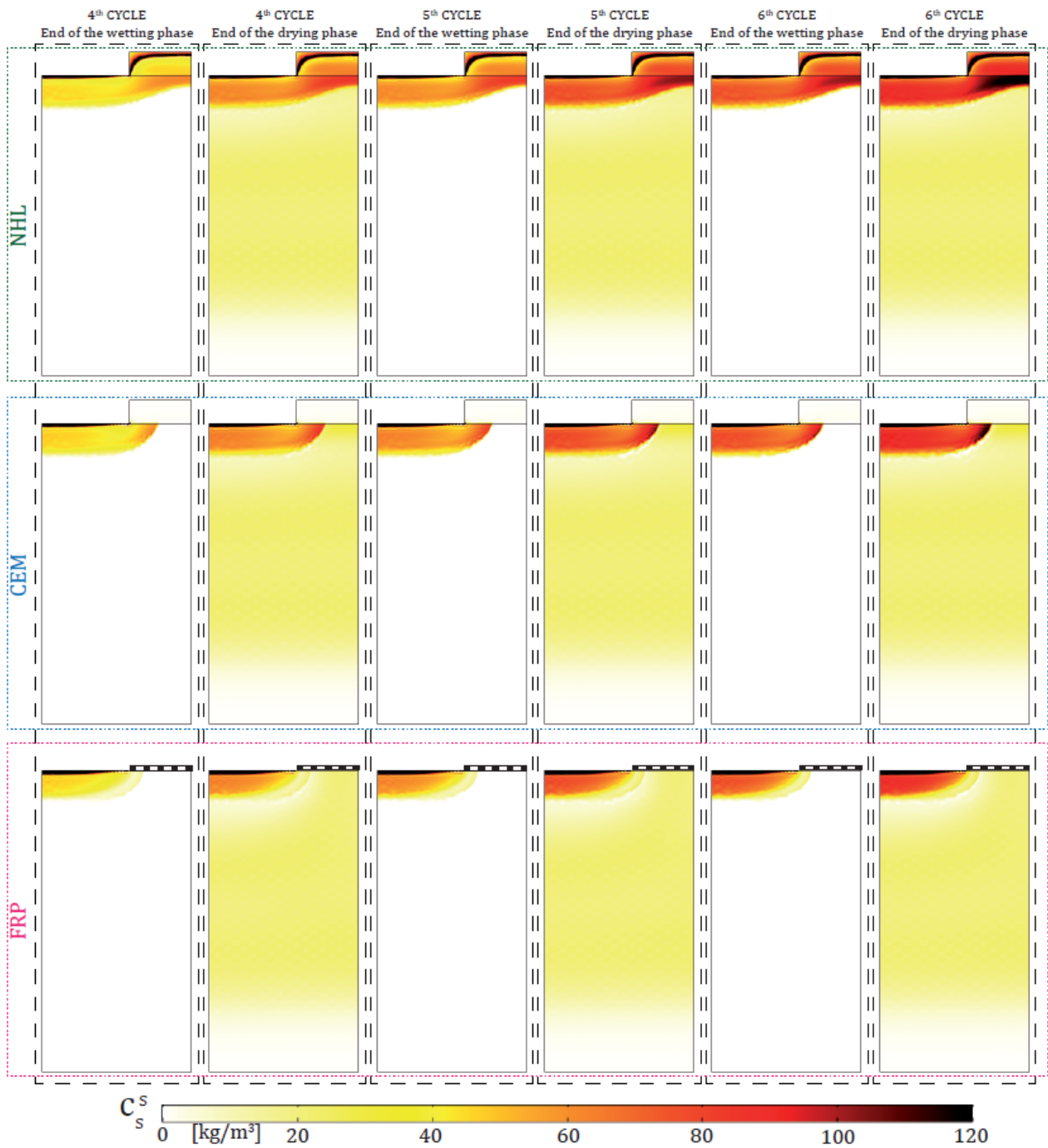


Fig. 14 – Comparison of the evolution of salt crystallization within specimens strengthened with different composite systems. Last three cycles.

Another key issue that could be examined by exploiting the model and the numerical procedure presented in the previous sections consists in understanding which are limit material properties of the composite matrix which could lead to a CEM-type behavior rather than an NHL-type behavior, i.e. understanding for which material properties no or limited salt crystallization arises in the composite matrix, when a FRCM-strengthened masonry specimen is subjected to conditioning. To this aim, a parametric analysis has been carried out following the material parameters settings collected in Table 3. In particular, the hygroscopic properties of three different materials (INT1, INT2 and INT3), which are not actual or existing materials, have been simply supposed by dividing the difference between the properties values of NHL and CEM (in terms of r_b , ϕ_0 , A

and K_s) into four evenly distributed intervals (Table 3). In this way, although INT1, INT2 and INT3 are not merely actual materials, this parametric analysis could show for which material properties setting the crystallized salt accumulation in the composite matrix is significantly limited as for the CEM case. It has to be pointed out that the four material properties considered in this parametric analysis (r_b , ϕ_0 , A and K_s) are actually physically interconnected as, for example, a variation of the mean pore radius of a material induces a variation of its water absorption and salt diffusion coefficients, and vice versa, as well as in the porosity of the material (that shows, however, a small variation between NHL and CEM cases).

Table 3. Parametric analysis on the mortar properties. The materials INT1, INT2 and INT3 are not actual materials.

Mortar	Mean pore radius r_b [μm]	Total open porosity ϕ_0 [%]	Water adsorption coef. A [$\text{kg}/\text{m}^2/\text{s}^{0.5}$]	Salt diffusion coef. K_s [m^2/s]
NHL	0.491 (from [28])	26.6% (from [28])	0.054 (from [28])	$0.120 \cdot 10^{-9}$ (from [51])
INT1	0.378	25.5%	0.045	$0.095 \cdot 10^{-9}$
INT2	0.266	24.5%	0.037	$0.070 \cdot 10^{-9}$
INT3	0.153	23.5%	0.028	$0.045 \cdot 10^{-9}$
CEM	0.041 (from [28])	22.5% (from [28])	0.020 (from [28])	$0.020 \cdot 10^{-9}$ (from [52])

The weathering procedure discussed in Section 3.4 has been also simulated by accounting for INT1, INT2 and INT3 composite matrixes. The evolution of crystallized salt in the composite matrix (point C of Fig. 4(b)) along with the weathering procedure is reported in Fig. 15 for INT1, INT2 and INT3 and compared with NHL and CEM. As can be noted in Fig. 15, although the material properties have been defined by dividing the difference between the properties values of NHL and CEM in evenly distributed intervals, the values of crystallized salt in INT1, INT2 and INT3 are not evenly distributed between the values of NHL and CEM along with the weathering procedure, evidently due to the nonlinear nature of the problem. Indeed, concerning the final value of crystallized salt in the composite matrix, c_s^S in the CEM case is about $2 \text{ kg}/\text{m}^3$, in the INT1 case is about $55 \text{ kg}/\text{m}^3$, in the INT2 case is about $28 \text{ kg}/\text{m}^3$, in the INT3 case is about $9 \text{ kg}/\text{m}^3$, and in the NHL case is about $85 \text{ kg}/\text{m}^3$.

As a result of this simple parametric analysis, the salt crystallization and accumulation in the composite matrix remains rather limited for the INT3 and CEM cases. In general, the mean pore radius (r_b) is the clearest hygroscopic parameter from a material producer point of view, as it could be directly and easily measured along with mix design choices. Therefore, although the mortar properties used in this parametric analysis are not relative to merely actual materials, a value of mean pore radius $r_b < 0.15 \mu\text{m}$ seems to prevent significant salt crystallization and accumulation in the composite matrix. This outcome could represent, indeed, a guideline to reduce (or even prevent) salt crystallization within the FRCM composite.

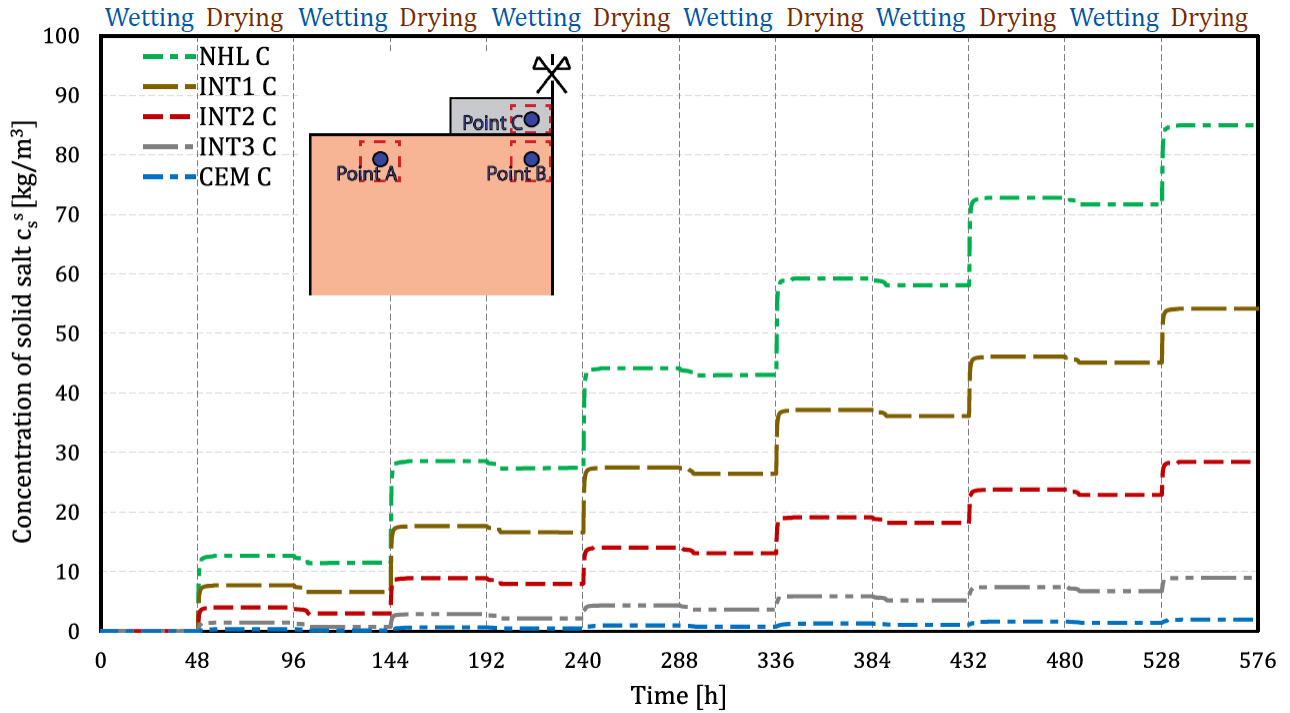


Fig. 15 – Parametric analysis on the composite matrix properties. Evolution of crystallized salt in the composite matrix (point C of Fig. 4(b)) along with the weathering procedure.

5 Conclusions

The simulation of accelerated ageing weathering cycles of masonry strengthened with composites has been carried out through a coupled multiphase model accounting for hygroscopic phenomena, salt transport and crystallization. Such model has been implemented together with ad hoc boundary conditions and a restart analysis procedure which attempted to reproduce the repetition of weathering cycles. In this way, laboratory accelerated weathering tests on masonry specimens strengthened with NHL-based FRCM have been numerically reproduced and additional information on the salt crystallization process within the specimen has been obtained along with the weathering procedure.

Further numerical insights have been shown and compared for different strengthening systems, namely CEM-based FRCM and FRP. The pattern of accumulation of crystallized salt in the specimens has been found sensibly different between the three strengthening systems. Particularly, crystallized salt accumulation has been found to occur in the top part of the NHL-based FRCM case likewise on the uncovered brick, brick portion beneath the composite matrix and composite matrix. Conversely, no significant crystallized salt accumulation has been observed in the brick portion beneath the composite for CEM-based FRCM and FRP cases. Additionally, no significant crystallized salt accumulation has been observed in the composite matrix in the CEM-based FRCM case.

Finally, limit material properties of the composite matrix which lead to a CEM-type behavior rather than an NHL-type behavior have been investigated through a parametric analysis. As a result, a value of mean pore radius $r_b < 0.15 \mu\text{m}$ seems to prevent significant salt crystallization and accumulation in the composite matrix. This outcome, although further investigation is needed to check if the same results are obtained with different salts used in the saline solution, appears interesting as could be directly accounted for to improve the durability of composites applied on masonry substrates. Indeed, the presence of crystallized salts in the composite matrix could negatively affect the durability of the material in two ways: (i) degradation of the porous matrix and (ii) corrosion of the fibers within the matrix (especially in the case of steel fibers).

It is worth to note that, although it is generally believed that more permeable is the composite applied on a masonry substrate, more durable is the composite system, the numerical investigation carried out in this paper highlighted that more permeable is the composite matrix, more salts are going to crystallize within the composite matrix threatening, thereby, the durability of the composite system itself.

Although accelerated laboratory weathering conditions have been considered in this paper, the multiphase model herein proposed allows, in general, also the simulation of on-site actual long-term environmental actions that can act on real buildings. Future research could be also focused on the estimation the effectiveness of accelerated laboratory weathering with respect to on-site conditions, through the proposed multiphase model.

Moreover, the potential of this multiphase model to predict the salt concentration in full-scale historical structures (also strengthened with composites) appears substantial. Indeed, simulations with standard workstations could be conducted up to real-scale masonry elements (e.g. piers), while other numerical strategies (e.g. multiscale analysis [37]) could be followed when the numerical modelling of whole historical structures is required.

Further developments could be addressed to the quantitative evaluation of the durability of composite strengthening systems applied on masonry substrates. To this aim, multiphysics approaches accounting also for mechanics (e.g. damage in the porous matrix) could be coupled with the multiphase modeling strategy developed in this paper. For example, the relationship proposed by Steiger [53, 54] which defines the crystallization pressure exerted by crystals growing in porous materials could be utilized.

Acknowledgements

Prof Christian Carloni is gratefully acknowledged for the supply of experimental data and the fruitful discussions and comments about this research. Financial support by the Italian Ministry of Education, Universities and Research MIUR is gratefully acknowledged (PRIN2015 “Advanced mechanical modeling of new materials and structures for the solution of 2020 Horizon challenges” prot. 2015JW9NJT_018).

Data availability

Data will be made available on request.

References

- [1] G. W. Scherer, “Stress from crystallization of salt,” *Cement and concrete research*, vol. 34, no. 9, pp. 1613-1624, 2004.
- [2] P. López-Arce, E. Doehne, J. Greenshields, D. Benavente and D. Young, “Treatment of rising damp and salt decay: the historic masonry buildings of Adelaide, South Australia,” *Materials and structures*, vol. 42, no. 6, pp. 827-848, 2009.
- [3] L. Falchi, D. Slanzi, E. Balliana, G. Driussi and E. Zendri, “Rising damp in historical buildings: A Venetian perspective,” *Building and Environment*, vol. 131, pp. 117-127, 2018.
- [4] B. Lubelli and M. R. de Rooij, “NaCl crystallization in restoration plasters,” *Construction and building Materials*, vol. 23, no. 5, pp. 1736-1742, 2009.

- [5] D. Watt and B. Colston, "Investigating the effects of humidity and salt crystallisation on medieval masonry," *Building and Environment*, vol. 35, no. 8, pp. 737-749, 2000.
- [6] B. Lubelli, R. P. van Hees and C. J. Groot, "The role of sea salts in the occurrence of different damage mechanisms and decay patterns on brick masonry," *Construction and building materials*, vol. 18, no. 2, pp. 119-124, 2004.
- [7] D. Benavente, L. Linares-Fernandez, G. Cultrone and E. Sebastian, "Influence of microstructure on the resistance to salt crystallisation damage in brick," *Materials and structures*, vol. 39, no. 1, pp. 105-113, 2006.
- [8] E. Franzoni, C. Gentilini, G. Graziani and S. Bandini, "Towards the assessment of the shear behaviour of masonry in on-site conditions: a study on dry and salt/water conditioned brick masonry triplets," *Construction and Building Materials*, vol. 65, pp. 405-416, 2014.
- [9] A. M. D'Altri, G. Castellazzi and S. de Miranda, "Collapse investigation of the Arquata del Tronto medieval fortress after the 2016 Central Italy seismic sequence," *Journal of Building Engineering*, vol. 18, pp. 245-251, 2018.
- [10] N. Reboul, Z. Mesticou, A. S. Larbi and E. Ferrier, "Experimental study of the in-plane cyclic behaviour of masonry walls strengthened by composite materials," *Construction and Building Materials*, vol. 164, pp. 70-83, 2018.
- [11] A. M. D'Altri, C. Carloni, S. de Miranda and G. Castellazzi, "Numerical modeling of FRP strips bonded to a masonry substrate," *Composite Structures*, vol. 200, pp. 420-433, 2018.
- [12] R. Fedele and G. Milani, "Assessment of bonding stresses between FRP sheets and masonry pillars during delamination tests," *Composites Part B: Engineering*, vol. 43, no. 4, pp. 1999-2011, 2012.
- [13] N. Galati, G. Tumialan and A. Nanni, "Strengthening with FRP bars of URM walls subject to out-of-plane loads," *Construction and Building Materials*, vol. 20, no. 1-2, pp. 101-110, 2006.
- [14] E. Grande, M. Imbimbo and E. Sacco, "Numerical investigation on the bond behavior of FRCM strengthening systems," *Composites Part B: Engineering*, vol. 145, pp. 240-251, 2018.
- [15] A. Bellini, M. Bovo and C. Mazzotti, "Experimental and numerical evaluation of fiber-matrix interface behaviour of different FRCM systems," *Composites Part B: Engineering*, vol. 161, p. 411-426, 2019.
- [16] S. Babaeidarabad, D. Arboleda, G. Loreto and A. Nanni, "Shear strengthening of un-reinforced concrete masonry walls with fabric-reinforced-cementitious-matrix," *Construction and Building Materials*, vol. 65, pp. 243-253, 2014.
- [17] E. Bertolesi, G. Milani, F. G. Carozzi and C. Poggi, "Ancient masonry arches and vaults strengthened with TRM, SRG and FRP composites: Numerical analyses," *Composite Structures*, vol. 187, pp. 385-402, 2018.

- [18] C. G. Papanicolaou, T. C. Triantafillou, K. Karlos and M. Papathanasiou, "Textile-reinforced mortar (TRM) versus FRP as strengthening material of URM walls: in-plane cyclic loading," *Materials and structures*, vol. 40, no. 10, pp. 1081-1097, 2007.
- [19] Z. Ullah, S. A. Grammatikos, M. C. Evernden and C. J. Pearce, "Multi-scale computational homogenisation to predict the long-term durability of composite structures," *Computers & Structures*, vol. 181, pp. 21-31, 2017.
- [20] "Linea Guida per la identificazione, la qualificazione ed il controllo di accettazione di compositi fibrorinforzati a matrice inorganica (FRCM) da utilizzarsi per il consolidamento strutturale di costruzioni esistenti," Consiglio Superiore dei Lavori Pubblici, 2018.
- [21] H. Maljaee, B. Ghiassi, P. Lourenço and D. Oliveira, "FRP-brick masonry bond degradation under hygrothermal conditions," *Composite Structures*, vol. 147, pp. 143-154, 2016.
- [22] M. Sciolti, M. Aiello and M. Frigione, "Effect of thermo-hygrometric exposure on frp, natural stone and their," *Composites Part B*, vol. 80, pp. 162-176, 2015.
- [23] M. Aiello, B. Ghiassi and P. Lourenço, "FRP-strengthened masonry," in *Long-term Performance and Durability of Masonry Structures*, Elsevier Ltd., 2019, pp. 209-238.
- [24] C. Gentilini, E. Franzoni, M. Santandrea and C. Carloni, "Salt-Induced Deterioration on FRP-Brick Masonry Bond," in *Structural Analysis of Historical Constructions*, Springer, Cham, 2019, pp. 1914-1921.
- [25] G. Cardani, M. R. Valluzzi, M. Panizza, P. Girardello and L. Binda, "Influence of salt crystallization on composites-to-masonry bond evaluated on site by pull-off tests," *Key Engineering Materials*, vol. 624, pp. 338-345, 2015.
- [26] E. Franzoni, C. Gentilini, M. Santandrea, S. Zanotto and C. Carloni, "Durability of steel FRCM-masonry joints: Effect of water and salt crystallization," *Materials and Structures*, vol. 50, no. 4, p. 201, 2017.
- [27] E. Franzoni, C. Gentilini, M. Santandrea and C. Carloni, "Effects of rising damp and salt crystallization cycles in FRCM-masonry interfacial debonding: Towards an accelerated laboratory test method," *Construction and Building Materials*, vol. 175, pp. 225-238, 2018.
- [28] E. Franzoni, M. Santandrea, C. Gentilini, A. Fregni and C. Carloni, "The role of mortar matrix in the bond behavior and salt crystallization resistance of FRCM applied to masonry," *Construction and Building Materials*, vol. 209, p. 592-605, 2019.
- [29] D. Gawin, B. A. Schrefler and M. Galindo, "Thermo-hydro-mechanical analysis of partially saturated porous materials," *Engineering Computations*, vol. 13, no. 7, pp. 113-143, 1996.
- [30] M. Koniorczyk and D. Gawin, "Heat and moisture transport in porous building materials containing salt," *Journal of Building Physics*, vol. 31, no. 4, pp. 279-300, 2008.

- [31] M. Koniorczyk and D. Gawin, “Numerical modeling of salt transport and precipitation in non-isothermal partially saturated porous media considering kinetics of salt phase changes,” *Transport in Porous Media*, vol. 87, no. 1, pp. 57-76, 2011.
- [32] M. Koniorczyk and D. Gawin, “Modelling of salt crystallization in building materials with microstructure–Poromechanical approach,” *Construction and Building Materials*, vol. 36, pp. 860-873, 2012.
- [33] M. Koniorczyk, D. Gawin and B. A. Schrefler, “Multiphysics model for spalling prediction of brick due to in-pore salt crystallization,” *Computers & Structures*, vol. 196, pp. 233-245, 2018.
- [34] H. Derluyn, P. Moonen and J. Carmeliet, “Deformation and damage due to drying-induced salt crystallization in porous limestone,” *Journal of the Mechanics and Physics of Solids*, vol. 63, pp. 242-255, 2014.
- [35] G. Castellazzi, C. Colla, S. de Miranda, G. Formica, E. Gabrielli, L. Molari and F. Ubertini, “A coupled multiphase model for hygrothermal analysis of masonry structures and prediction of stress induced by salt crystallization,” *Construction and Building Materials*, vol. 41, p. 717–731, 2013.
- [36] G. Castellazzi, S. de Miranda, L. Gremontieri, L. Molari and F. Ubertini, “Multiphase model for hygrothermal analysis of porous media with salt crystallization and hydration,” *Materials and Structures*, vol. 49, no. 3, p. 1039–1063, 2015.
- [37] G. Castellazzi, S. de Miranda, G. Formica, L. Molari and F. Ubertini, “Coupled hygro-mechanical multiscale analysis of masonry walls,” *Engineering Structures*, vol. 84, pp. 266-278, 2015.
- [38] L. Gremontieri, F. Daghia, L. Molari, G. Castellazzi, H. Derluyn, V. Cnudde and S. de Miranda, “A multi-scale approach for the analysis of the mechanical effects of salt crystallisation in porous media,” *International Journal of Solids and Structures*, vol. 126, pp. 225-239, 2017.
- [39] M. W. Lin, J. B. Berman, M. Khoshbakht, C. A. Feickert and A. O. Abatan, “Modeling of moisture migration in an FRP reinforced masonry structure,” *Building and Environment*, vol. 41, no. 5, pp. 646-656, 2006.
- [40] M. Khoshbakht, M. W. Lin and C. A. Feickert, “A finite element model for hygrothermal analysis of masonry walls with FRP reinforcement,” *Finite Elements in Analysis and Design*, vol. 45, no. 8-9, pp. 511-518, 2009.
- [41] M. Khoshbakht and M. W. Lin, “A finite element model for hygro-thermo-mechanical analysis of masonry walls with FRP reinforcement,” *Finite Elements in Analysis and Design*, vol. 46, no. 10, pp. 783-791, 2010.
- [42] R. M. Espinosa, L. Franke and G. Deckelmann, “Phase changes of salts in porous materials: crystallization, hydration and deliquescence,” *Construction and Building Materials*, vol. 22, no. 8, pp. 1758-1773, 2008.
- [43] M. Koniorczyk and P. Konca, “Experimental and numerical investigation of sodium sulphate crystallization in porous materials,” *Heat and Mass Transfer*, vol. 49, no. 3, p. 437–449, 2013.

- [44] L. Grementieri, L. Molari, H. Derluyn, J. Desarnaud, V. Cnudde, N. Shahidzadeh and S. de Miranda, “Numerical simulation of salt transport and crystallization in drying Prague sandstone using an experimentally consistent multiphase model,” *Building and Environment*, vol. 123, p. 289–298, 2017.
- [45] J. Sýkora, T. Krejčí, J. Kruis and M. Šejnoha, “Computational homogenization of non-stationary transport processes in masonry structures,” *Journal of Computational and Applied Mathematics*, vol. 236, no. 18, pp. 4745–4755, 2012.
- [46] *COMSOL multiphysics modeling guide*, 2016.
- [47] B. Lubelli, V. Cnudde, T. Diaz-Goncalves, E. Franzoni, R. P. J. van Hees, I. Ioannou, B. Menendez, C. Nunes, H. Siedel, M. Stefanidou, V. Verges-Belmin and H. Viles, “Towards a more effective and reliable salt crystallization test for porous building materials: state of the art,” *Materials and Structures*, vol. 51, no. 55, pp. 1–21, 2018.
- [48] B. Simon, “Dissolution rates of NaCl and KCl in aqueous solution,” *Journal of Crystal Growth*, vol. 52, p. 789–794, 1981.
- [49] N. Shahidzadeh-Bonn, J. Desarnaud, F. Bertrand, X. Chateau and D. Bonn, “Damage in porous media due to salt crystallization,” *Physical Review E*, vol. 81, no. 6, 2010.
- [50] J. Ahl, “Salt diffusion in brick structures Part II The effect of temperature, concentration and salt,” *Journal of materials science*, vol. 39, no. 13, pp. 4247–4254, 2004.
- [51] K. Akrouf, M. Ltifi and M. B. Ouezdou, “Chloride Diffusion in Mortars—Effect of the Use of Limestone Sand Part II: Immersion Test,” *International Journal of Concrete Structures and Materials*, vol. 4, no. 2, pp. 109–112, 2010.
- [52] O. M. Jensen, P. F. Hansen, A. M. Coats and F. P. Glasser, “Chloride ingress in cement paste and mortar,” *Cement and Concrete Research*, vol. 29, no. 9, pp. 1497–1504, 1999.
- [53] M. Steiger, “Crystal growth in porous materials—I: The crystallization pressure of large crystals,” *Journal of Crystal Growth*, vol. 282, no. 3–4, p. 455–469, 2005.
- [54] M. Steiger, “Crystal growth in porous materials—II: Influence of crystal size on the crystallization pressure,” *Journal of Crystal Growth*, vol. 282, no. 3–4, p. 470–481, 2005.